3D LEAST SQUARES MATCHING APPLIED TO MICRO-TOMOGRAPHY DATA

F. Liebold[1]*, R. Lorenzoni[2], I. Curosu[3], F. Léonard[4], V. Mechtcherine[3], S. Paciornik[2], H.-G. Maas[1]

[1] Institute of Photogrammetry and Remote Sensing, Technische Universität Dresden, Germany -
(frank.liebold, hans-gerd.maas)@tu-dresden.de
[2] Department of Chemical and Materials Engineering, Pontifícia Universidade Católica do Rio de Janeiro (PUC-Rio),
Rio de Janeiro, Brazil - renata.lorenzoni@aluno.puc-rio.br, sidnei@puc-rio.br
[3] Institute of Construction Materials, Technische Universität Dresden, Germany -
(iurie.curosu, viktor.mechtcherine)@tu-dresden.de
[4] University of Manchester at Harwell, Diamond Light Source, Harwell Science & Innovation Campus,
Didcot, Oxfordshire OX11 0DE UK - fabien.leonard@manchester.ac.uk

Commission II, WG II/5

KEY WORDS: 3D Least Squares Matching, Cuboid Tracking, Displacement Vector Field, Material Testing, Computed Tomography, In-situ Test.

ABSTRACT:

The paper introduces 3D least squares matching as a technique to analyze multi-temporal micro-tomography data in civil engineering material testing. Time series of tomography voxel data sets are recorded during an in-situ tension test of a strain-hardening cement-based composite probe at consecutive load steps. 3D least squares matching is a technique to track cuboids in consecutive voxel data sets minimizing the sum of the squares of voxel value differences after a 12-parameter 3D affine transformation. For a regular grid of locations in each voxel data set of the deformed states, a subvoxel-precise 3D displacement vector field is computed. Discontinuities in these displacement vector fields indicate the occurrence of cracks in the probes during the load tests. These cracks are detected and quantitatively described by the computation of principal strains of tetrahedrons in a tetrahedral mesh, that is generated between the matching points. The subvoxel-accuracy potential of the technique allows the detection of very small cracks with a width much smaller than the actual voxel size.

1. INTRODUCTION

In materials research, several measurement techniques are used. Classical instruments, that allow the observation of surfaces of specimens, are for example strain gauges, inductive displacement transducers or inclinometers. In the last years, photogrammetric camera systems also became more and more part of the facilities of research labs with the advantage of being contactless and having a high spatial resolution and accuracy. Most photogrammetric contributions in this field use image sequences of camera systems and apply digital image correlation (DIC) techniques in order to compute displacement vector fields and use them for further analysis (Hampel and Maas, 2003, Maas and Hampel, 2006, Hampel and Maas, 2009, Sutton et al., 2009, Barazzetti and Scaioni, 2010, Koschitzki et al., 2011, Liebold and Maas, 2016, Liebold and Maas, 2018, Liebold et al., 2019, Liebold and Maas, 2020, Liebold et al., 2020a, Liebold et al., 2020b). Early applications of DIC were based on the cross-correlation method (Barnea and Silverman, 1972). Later, gradient based techniques were developed (Lucas and Kanade, 1981). These techniques used an iterative least squares algorithm to compute the displacements. (Ackermann, 1984) and (Grün, 1985) extended the mathematical model to an affine transform where rotation, scaling and shearing were considered. However, DIC techniques applied to image sequences only allow the observation of a specimen's surface. A further interesting point is the view inside the specimen. Therefor, X-ray tomography can be used. During load tests, a specimen can be observed in an in-situ experiment where different states of deformation are recorded in a tomograph. The above-

mentioned 2D techniques can be extended to 3D and are then called digital volume correlation (DVC). (Bay et al., 1999) applied 3D cross-correlation to X-ray tomography data in order to compute 3D displacement vector fields. While 3D cross-correlation determines three shift parameters between consecutive cuboids of voxel data, (Maas et al., 1994) described a subvoxel-precise 12-parameter 3D least-squares cuboid tracking applied to a sequence of 3D images taken from two mixed fluids. The mathematical model was an affine transform that included translation, rotation, scale as well as shear parameters. The paper at hand is based on the work of (Maas et al., 1994) and will extend the mathematical model with radiometric parameters. The algorithm will be applied to data sets of different deformation states from an in-situ tension test with a fiber-reinforced composite probe (strain-hardening cement-based composite, SHCC). The data was recorded by a micro-CT instrument and the experiment is described in (Lorenzoni et al., 2020). Fig. 1 shows one slice of the voxel data of the reference state as well as one slice of a deformed state from the experiment. In the deformed state, cracks are clearly visible.

The paper is structured as follows: Section 2 gives an overview of the 3D least squares matching algorithm. Then, section 3 shows the analysis of the displacement fields using the strain analysis. At the end, a conclusion is given.

2. 3D LEAST SQUARES MATCHING

2.1 Mathematical Model

The 3D least squares matching (3D LSM) algorithm is applied to two volume data sets. In the reference volume, the integer
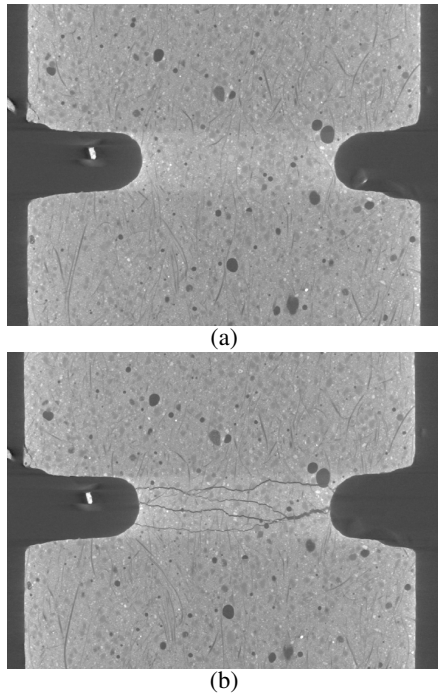
---

* Corresponding author

(a)

(b)

Figure 1. a: One image of the image stack of the volume in the reference epoch; b: One image of the image stack of the volume in the later deformed epoch where cracks can be seen.

coordinates $x_{Ref,c}$, $y_{Ref,c}$, $z_{Ref,c}$ of the point to be matched are given which are the center of a small cuboid with defined odd dimensions dim_x, dim_y and dim_z:

$$
\begin{aligned}
x_{Ref} &\in [x_{Ref,c} - h_x, x_{Ref,c} + h_x] \quad \wedge \quad x_{Ref} \in \mathbb{N} \\
y_{Ref} &\in [y_{Ref,c} - h_y, y_{Ref,c} + h_y] \quad \wedge \quad y_{Ref} \in \mathbb{N} \\
z_{Ref} &\in [z_{Ref,c} - h_z, z_{Ref,c} + h_z] \quad \wedge \quad z_{Ref} \in \mathbb{N}
\end{aligned}
\tag{1}
$$

where $\quad h_x = \frac{dim_x - 1}{2}; h_y = \frac{dim_y - 1}{2}; h_z = \frac{dim_z - 1}{2}$

The aim is to find the corresponding subvolume with the coordinates $x_{Def}, y_{Def}, z_{Def}$ in the second volume of the deformed state. Eq. 2 shows the relationship between the gray values of the first (reference) and second (deformed) volume, also taking into account radiometric parameters (r_0, r_1):

$$
f(x_{Ref}, y_{Ref}, z_{Ref}) = r_0 + r_1 \cdot g(x_{Def}, y_{Def}, z_{Def}) \tag{2}
$$

where $\quad f(x_{Ref}, y_{Ref}, z_{Ref})$ = gray value (reference state)
$g(x_{Def}, y_{Def}, z_{Def})$ = gray value (deformed state)

Eq. 2 is valid for all voxels in the cuboid. Between the two states, a coordinate transformation is applied. Similar to (Ackermann, 1984) and (Maas et al., 1994), a 3D affine transformation is used containing displacements, rotations, shear and scaling, see Eq. 3. The shifts are represented by a_0, b_0 and c_0.

$$
\begin{aligned}
x_{Def} &= x_{Ref,c} + a_0 + a_1 \cdot \tilde{x} + a_2 \cdot \tilde{y} + a_3 \cdot \tilde{z} \\
y_{Def} &= y_{Ref,c} + b_0 + b_1 \cdot \tilde{x} + b_2 \cdot \tilde{y} + b_3 \cdot \tilde{z} \\
z_{Def} &= z_{Ref,c} + c_0 + c_1 \cdot \tilde{x} + c_2 \cdot \tilde{y} + c_3 \cdot \tilde{z}
\end{aligned}
\tag{3}
$$

where $\quad a_i, b_i, c_i$ = affine parameters
$\tilde{x} = x_{Ref} - x_{Ref,c}$, reduced x coordinate
$\tilde{y} = y_{Ref} - y_{Ref,c}$, reduced y coordinate
$\tilde{z} = z_{Ref} - z_{Ref,c}$, reduced z coordinate

Thus, the vector of unknowns is:

$$
\mathbf{p} = (\; a_0, \; a_1, \; a_2, \; a_3, \; b_0, \; b_1, \\
\quad b_2, \; b_3, \; c_0, \; c_1, \; c_2, \; c_3, \; r_0, \; r_1 \;)^T \tag{4}
$$

$\mathbf{p}$ has 14 unknowns and the cuboid contains at least $3 \times 3 \times 3 = 27$ voxels (usually more), so that there is an over-determination. Thus, the parameters of $\mathbf{p}$ are computed using the least squares method. Therefore, a residuum is added to Eq. 2 in order to get the observation equation:

$$
\begin{aligned}
f(x_{Ref}, y_{Ref}, z_{Ref}) + v(x_{Ref}, y_{Ref}, z_{Ref}) = \\
r_0 + r_1 \cdot g(x_{Def}, y_{Def}, z_{Def})
\end{aligned}
\tag{5}
$$

where $\quad v(x_{Ref}, y_{Ref}, z_{Ref})$ = residuum

The linearization of the observation equation is done using the first terms of the Taylor series:

$$
\begin{aligned}
f(x_{Ref}, y_{Ref}, z_{Ref}) + v(x_{Ref}, y_{Ref}, z_{Ref}) \approx \\
r_{0,0} + \mathrm{d}r_0 + (r_{1,0} + \mathrm{d}r_1) \cdot g(x_{Def,0}, y_{Def,0}, z_{Def,0}) \\
+ r_{1,0} \cdot (g_x \cdot \mathrm{d}x_{Def} + g_y \cdot \mathrm{d}y_{Def} + g_z \cdot \mathrm{d}z_{Def})
\end{aligned}
\tag{6}
$$

where $\quad x_{Def,0}$ = x computed with initial values of a_i
$y_{Def,0}$ = y computed with initial values of b_i
$z_{Def,0}$ = z computed with initial values of c_i
$r_{0,0}, r_{1,0}$ = initial values of r_0, r_1

The gray value $g(x_{Def,0}, y_{Def,0}, z_{Def,0})$ is computed by trilinear interpolation at the position $(x_{Def,0}, y_{Def,0}, z_{Def,0})$. Eq. 6 also contains derivations: the volume gradients of the gray values.

$$
\begin{aligned}
g_x &= \frac{\partial g(x_{Def}, y_{Def}, z_{Def})}{\partial x_{Def}} \Big|_{x_{Def,0}, y_{Def,0}, z_{Def,0}} \\
g_y &= \frac{\partial g(x_{Def}, y_{Def}, z_{Def})}{\partial y_{Def}} \Big|_{x_{Def,0}, y_{Def,0}, z_{Def,0}} \\
g_z &= \frac{\partial g(x_{Def}, y_{Def}, z_{Def})}{\partial z_{Def}} \Big|_{x_{Def,0}, y_{Def,0}, z_{Def,0}}
\end{aligned}
\tag{7}
$$

They can be obtained by a combination of numerical differentiation $g_{x,i}$, $g_{y,i}$, $g_{z,i}$ at the integer positions x_i, y_i, z_i (central differences, Eq. 8) and tri-linear interpolation.

$$
\begin{aligned}
g_{x,i} &\approx 0.5 \cdot (g(x_i + 1, y_i, z_i) - g(x_i - 1, y_i, z_i)) \\
g_{y,i} &\approx 0.5 \cdot (g(x_i, y_i + 1, z_i) - g(x_i, y_i - 1, z_i)) \\
g_{z,i} &\approx 0.5 \cdot (g(x_i, y_i, z_i + 1) - g(x_i, y_i, z_i - 1))
\end{aligned}
\tag{8}
$$

The differentials $\mathrm{d}x_{Def}$, $\mathrm{d}y_{Def}$ and $\mathrm{d}z_{Def}$ are computed by:

$$\mathrm{d}x_{Def} = \sum_{i=0}^{3} \frac{\partial x_{Def}}{\partial a_i} \cdot \mathrm{d}a_i = \begin{pmatrix} 1 \\ \tilde{x} \\ \tilde{y} \\ \tilde{z} \end{pmatrix}^T \cdot \begin{pmatrix} \mathrm{d}a_0 \\ \mathrm{d}a_1 \\ \mathrm{d}a_2 \\ \mathrm{d}a_3 \end{pmatrix}$$

$$\mathrm{d}y_{Def} = \sum_{i=0}^{3} \frac{\partial y_{Def}}{\partial b_i} \cdot \mathrm{d}b_i = \begin{pmatrix} 1 \\ \tilde{x} \\ \tilde{y} \\ \tilde{z} \end{pmatrix}^T \cdot \begin{pmatrix} \mathrm{d}b_0 \\ \mathrm{d}b_1 \\ \mathrm{d}b_2 \\ \mathrm{d}b_3 \end{pmatrix} \qquad (9)$$

$$\mathrm{d}z_{Def} = \sum_{i=0}^{3} \frac{\partial z_{Def}}{\partial c_i} \cdot \mathrm{d}c_i = \begin{pmatrix} 1 \\ \tilde{x} \\ \tilde{y} \\ \tilde{z} \end{pmatrix}^T \cdot \begin{pmatrix} \mathrm{d}c_0 \\ \mathrm{d}c_1 \\ \mathrm{d}c_2 \\ \mathrm{d}c_3 \end{pmatrix}$$

Thus, the vector of corrections to the unknowns is:

$$\mathrm{d}\mathbf{p} = (\begin{array}{cccccc} \mathrm{d}a_0, & \mathrm{d}a_1, & \mathrm{d}a_2, & \mathrm{d}a_3, & & \\ \mathrm{d}b_0, & \mathrm{d}b_1, & \mathrm{d}b_2, & \mathrm{d}b_3, & & \\ \mathrm{d}c_0, & \mathrm{d}c_1, & \mathrm{d}c_2, & \mathrm{d}c_3, & \mathrm{d}r_0, & \mathrm{d}r_1 \end{array})^T \qquad (10)$$

The vector of unknowns is composed of the vector of the initial values $\mathbf{p}_0$ and the vector of the corrections to the unknowns:

$$\mathbf{p} = \mathbf{p}_0 + \mathrm{d}\mathbf{p} \qquad (11)$$

The linearized observation equations can be written in matrix notation:

$$\mathbf{A} \cdot \mathrm{d}\mathbf{p} = \mathbf{l} + \mathbf{v} \qquad (12)$$

where $\mathbf{A}$ = Jacobian matrix
  $\mathbf{l}$ = reduced observation vector
  $\mathbf{v}$ = residual vector

The computation of the Jacobian matrix is shown in Eq. 13 and Eq. 14 shows the reduced observation vector.

$$\mathbf{l} = \begin{pmatrix} f_1 - r_0 - r_1 \cdot g_1 \\ f_2 - r_0 - r_1 \cdot g_2 \\ \vdots \end{pmatrix} \qquad (14)$$

In the Gauss-Markov model, the sum of the squares of the residuals is minimized:

$$\mathbf{v}^T \cdot \mathbf{v} \to \min_{\mathrm{d}\mathbf{p}} \qquad (15)$$

To achieve this, the normal equations are solved for $\mathrm{d}\mathbf{p}$:

$$\mathbf{A}^T \cdot \mathbf{A} \cdot \mathrm{d}\mathbf{p} = \mathbf{A}^T \cdot \mathbf{l} \qquad (16)$$

The corrections to the unknowns are added to the initial values using Eq. 11. The steps from Eq. 13 to Eq. 16 (and $\mathbf{p} = \mathbf{p}_0 + \mathrm{d}\mathbf{p}$) are repeated until the process converges.

$$\mathbf{A} = \left(\begin{array}{ccc} \left.\frac{\partial f}{\partial a_0}\right|_{\mathbf{p}=\mathbf{p}_0} & \left.\frac{\partial f}{\partial a_1}\right|_{\mathbf{p}=\mathbf{p}_0} & \cdots \\ \left.\frac{\partial f}{\partial a_2}\right|_{\mathbf{p}=\mathbf{p}_0} & \left.\frac{\partial f}{\partial a_3}\right|_{\mathbf{p}=\mathbf{p}_0} & \\ \left.\frac{\partial f}{\partial b_0}\right|_{\mathbf{p}=\mathbf{p}_0} & \left.\frac{\partial f}{\partial b_1}\right|_{\mathbf{p}=\mathbf{p}_0} & \\ \left.\frac{\partial f}{\partial b_2}\right|_{\mathbf{p}=\mathbf{p}_0} & \left.\frac{\partial f}{\partial b_3}\right|_{\mathbf{p}=\mathbf{p}_0} & \\ \left.\frac{\partial f}{\partial c_0}\right|_{\mathbf{p}=\mathbf{p}_0} & \left.\frac{\partial f}{\partial c_1}\right| & \\ \left.\frac{\partial f}{\partial c_2}\right|_{\mathbf{p}=\mathbf{p}_0} & \left.\frac{\partial f}{\partial c_3}\right|_{\mathbf{p}=\mathbf{p}_0} & \\ \left.\frac{\partial f}{\partial r_0}\right|_{\mathbf{p}=\mathbf{p}_0} & \left.\frac{\partial f}{\partial r_1}\right|_{\mathbf{p}=\mathbf{p}_0} & \end{array} \right) = \begin{pmatrix} r_1 \cdot g_{x1} & r_1 \cdot g_{x1} \cdot \tilde{x}_1 & r_1 \cdot g_{x1} \cdot \tilde{y}_1 & r_1 \cdot g_{x1} \cdot \tilde{z}_1 & r_1 \cdot g_{y1} & r_1 \cdot g_{y1} \cdot \tilde{x}_1 & r_1 \cdot g_{y1} \cdot \tilde{y}_1 & r_1 \cdot g_{y1} \cdot \tilde{z}_1 & r_1 \cdot g_{z1} & r_1 \cdot g_{z1} \cdot \tilde{x}_1 & r_1 \cdot g_{z1} & r_1 \cdot g_{z1} \cdot \tilde{y}_1 & r_1 \cdot g_{z1} \cdot \tilde{x}_1 & 1 & g_1 \\ r_1 \cdot g_{x2} & r_1 \cdot g_{x2} \cdot \tilde{y}_2 & r_1 \cdot g_{x2} \cdot \tilde{x}_2 & r_1 \cdot g_{x2} \cdot \tilde{z}_2 & r_1 \cdot g_{y2} & r_1 \cdot g_{y2} \cdot \tilde{x}_2 & r_1 \cdot g_{y2} \cdot \tilde{y}_2 & r_1 \cdot g_{y2} \cdot \tilde{z}_2 & r_1 \cdot g_{z2} & r_1 \cdot g_{z2} \cdot \tilde{x}_2 & r_1 \cdot g_{z2} & r_1 \cdot g_{z2} \cdot \tilde{y}_2 & r_1 \cdot g_{z2} \cdot \tilde{x}_2 & 1 & g_2 \\ \cdots & \cdots & \cdots & \cdots & \cdots & \cdots & \cdots & \cdots & \cdots & \cdots & \cdots & \cdots & \cdots & \cdots & \cdots \end{pmatrix}$$

$$(13)$$

The standard deviation of the unit weight is:

$$s_0 = \sqrt{\frac{\mathbf{v}^T \cdot \mathbf{v}}{n - u}} \qquad (17)$$

where $\quad \mathbf{v} = \mathbf{A} \cdot d\mathbf{p} - \mathbf{l}$ = residual vector
$\quad n$ = number of observations
$\quad u$ = number of unknowns

In addition, the standard deviation of the ith parameter is:

$$s_{p,i} = s_0 \cdot \sqrt{\mathbf{Q}_{xx,ii}} \qquad (18)$$

where $\quad \mathbf{Q}_{xx} = (\mathbf{A}^T \cdot \mathbf{A})^{-1}$ = cofactor matrix of unknowns

2.2 Initial Values

Due to the non-linearity of the gray value distribution in the volume data, initial values have to be obtained for the 3D LSM algorithm if the movements between the epochs exceed the dimensions of the cuboid. In case of predominant translations and small rotations, 3D cross-correlation can be used to compute initial shifts.

2.3 Application in the Experiment

As explained in the introduction part, the 3D least squares matching method is applied to a sequence of voxel data sets of a reference and six consecutive load levels. First, a regular 3D grid of points is defined, and points with insufficient contrast in their neighborhood are excluded. Before applying the least squares method, initial values are computed using 3D cross-correlation (Bay et al., 1999). Then, the displacement vector fields are computed using the 3D least squares matching algorithm. Fig. 2 shows a sequence of six displacement vector fields between the reference state and the deformed states. With higher loads (higher steps), cracks appear and grow. This also leads to higher differences between parts of the displacement vector fields.

To evaluate the influence of the affine and the radiometric parameters, the algorithm is applied introducing 3 (only translation), 12 (affine transformation) and 14 parameters (affine transformation and radiometric parameters) in the least squares process. The mean standard deviations of unit weight (Eq. 17) of the matching results are compared for the three versions and for each epoch, see Table 1. The differences in the s_0 values are less than 2 %. Between the epochs in the experiment, there are only very small rotations and also the radiometric conditions are almost the same such that there is no significant advantage to use 12 or 14 parameters. However, for other experiments, it may improve the results.

In addition, the precision is analyzed: Table 2 shows the mean standard deviations of the three translation parameters using Eq. 18 (cuboid dimensions $15 \times 15 \times 15$ vx). The precision values are consistently in the order of 0.01 to 0.02 vx.

epoch	mean($s_{0,t}$)	mean($s_{0,a}$)	mean($s_{0,r}$)
0→1	3.105	3.096	3.067
0→2	3.174	3.160	3.109
0→3	3.187	3.168	3.127
0→4	3.213	3.189	3.140
0→5	3.258	3.215	3.161
0→6	3.288	3.235	3.168

Table 1. Mean standard deviations of the unit weight of a 3-parameter computation $s_{0,t}$ (only shifts), a 12-parameter computation $s_{0,a}$ (affine parameters) and a 14-parameter computation $s_{0,r}$ (including radiometric parameters).

epoch	mean(s_{a_0})	mean(s_{b_0})	mean(s_{c_0})
0→1	0.0132 vx	0.0141 vx	0.0149 vx
0→2	0.0136 vx	0.0145 vx	0.0152 vx
0→3	0.0136 vx	0.0146 vx	0.0153 vx
0→4	0.0137 vx	0.0147 vx	0.0154 vx
0→5	0.0138 vx	0.0148 vx	0.0155 vx
0→6	0.0139 vx	0.0149 vx	0.0156 vx

Table 2. Mean standard deviations of the shift parameters in vx (14-parameter computation).

3. DEFORMATION ANALYSIS

In our material testing approach, it is important to find the discontinuities in the 3D displacement vector field. The computation of strains allows to identify such areas. The method that will be presented in Sec. 3.1 requires at least four points and the corresponding shifts to calculate a strain. Because of that, the points of the displacement vector field are triangulated into a tetrahedral mesh and for each tetrahedron, strains are computed. Fig. 3 shows a tetrahedral mesh of the probe of Fig. 1.

3.1 Strain Analysis

This section gives a short overview of the calculation of principal strains as well as volume strains in tetrahedral meshes as an extension of the 2D triangle analysis approach presented in (Liebold and Maas, 2016). The principal strains of tetrahedrons are computed using the coordinates of its vertices in the reference (x_{Ref}, y_{Ref}, z_{Ref}) and in the deformed state (x_{Def}, y_{Def}, z_{Def}). First, the parameters of an affine transformation between the coordinates are calculated using the four vertices of the tetrahedron.

$$\vec{p}_{Def} = \vec{t} + \mathbf{F} \cdot \vec{p}_{Ref}$$

$$\begin{pmatrix} x_{Def} \\ y_{Def} \\ z_{Def} \end{pmatrix} = \begin{pmatrix} t_1 \\ t_2 \\ t_3 \end{pmatrix} + \begin{pmatrix} f_{11} & f_{12} & f_{13} \\ f_{21} & f_{22} & f_{23} \\ f_{31} & f_{32} & f_{33} \end{pmatrix} \cdot \begin{pmatrix} x_{Ref} \\ y_{Ref} \\ z_{Ref} \end{pmatrix} \qquad (19)$$

where $\quad t_i, f_{ij}$ = affine parameters

The deformation gradient $\mathbf{F}$ is composed of the nine parameters f_{ij}. $\mathbf{F}$ can be decomposed into a product of a symmetric and rotation matrix (Becker and Bürger, 1975).

$$\mathbf{F} = \begin{pmatrix} f_{11} & f_{12} & f_{13} \\ f_{21} & f_{22} & f_{23} \\ f_{31} & f_{32} & f_{33} \end{pmatrix} = \mathbf{V} \cdot \mathbf{R} \qquad (20)$$

where $\quad \mathbf{F}$ = deformation gradient tensor
$\quad \mathbf{R}$ = rotation matrix
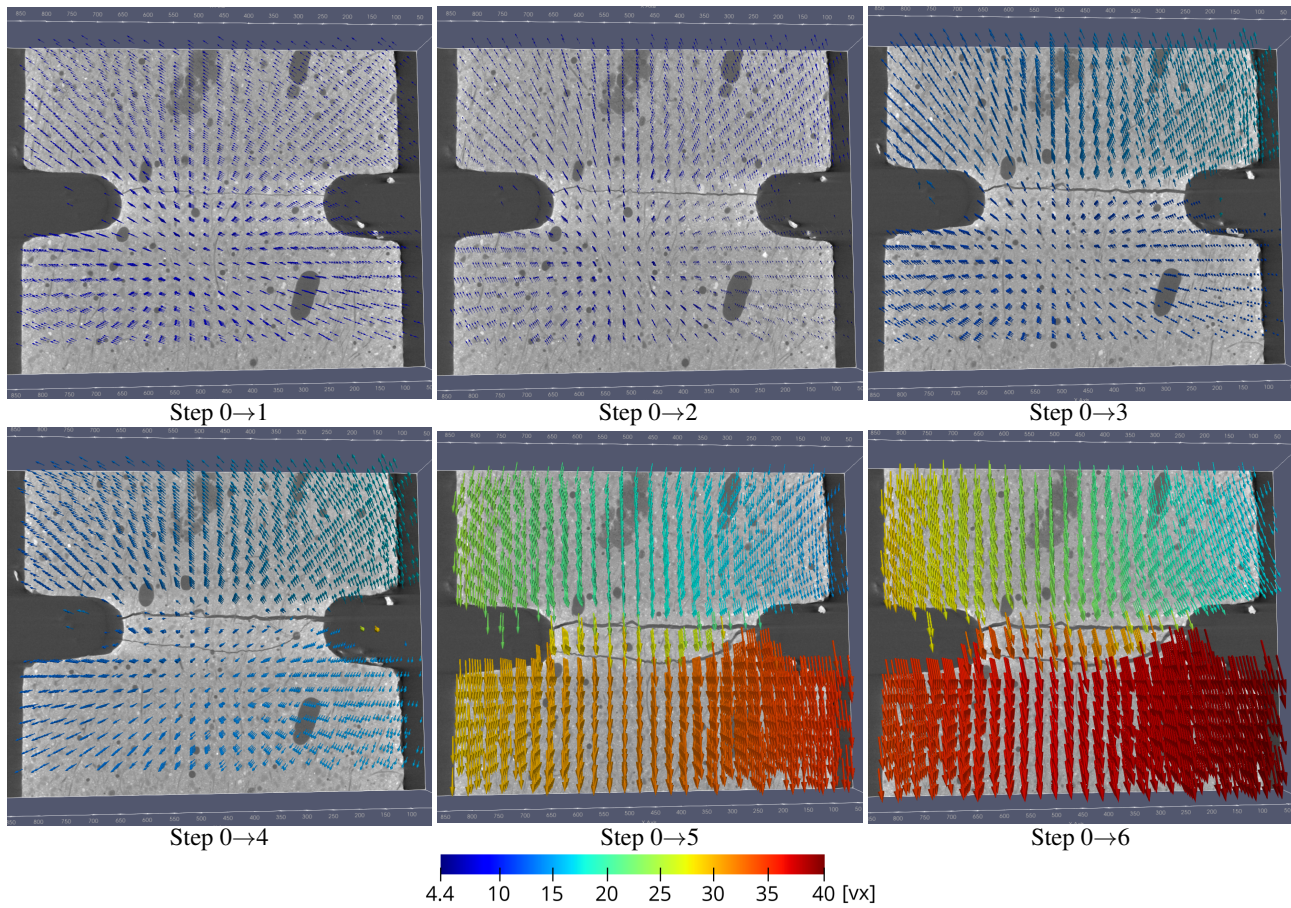$\quad \mathbf{V}$ = left stretch tensor (symmetric)

Figure 2. Color-coded visualizations of displacement vector fields of the different epochs (one layer of voxel data, 2D projections of 3D vectors).
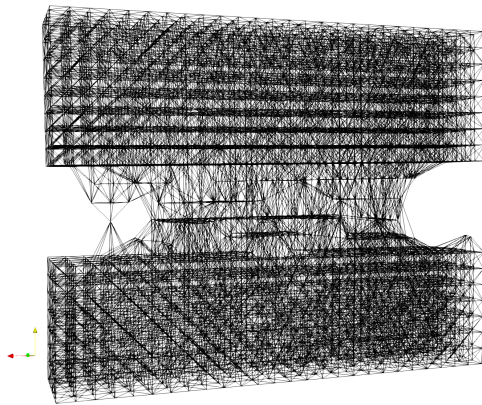

Figure 3. Tetrahedral mesh of the matching points.

The left Cauchy-Green deformation tensor $\mathbf{V}^2$ is calculated in order to compute the polar decomposition:

$$\mathbf{V}^2 = \mathbf{V} \cdot \mathbf{V}^T = \mathbf{F} \cdot \mathbf{F}^T \qquad (21)$$

In the next step, an eigenvalue decomposition of left Cauchy-Green deformation tensor is performed:

$$\mathbf{V}^2 = \mathbf{C} \cdot \mathbf{\Lambda} \cdot \mathbf{C}^T = \mathbf{C} \cdot \begin{pmatrix} \lambda_1 & 0 & 0 \\ 0 & \lambda_2 & 0 \\ 0 & 0 & \lambda_3 \end{pmatrix} \cdot \mathbf{C}^T \qquad (22)$$

where

$\mathbf{C}$ = eigenvector matrix (orthogonal matrix)
$\mathbf{\Lambda}$ = eigenvalue matrix (diagonal matrix)
$\lambda_i = i^{th}$ eigenvalue, diagonal element of $\mathbf{\Lambda}$
and $\lambda_1 \leq \lambda_2 \leq \lambda_3$

The greatest principal strain ϵ_3 (technical strain) is derived from the eigenvalue λ_3 (Eq. 23). It is a dimensionless quantity.

$$\epsilon_3 = \sqrt{\lambda_3} - 1 \qquad (23)$$

From $\mathbf{F}$, it is also possible to derive a volume strain (Ogden, 1997, Altenbach, 2018):

$$\epsilon_v = det(\mathbf{F}) - 1 \qquad (24)$$

A crack crossing a tetrahedron will cause an extension of the tetrahedron and will thus lead to a larger value of ϵ_3 as well as ϵ_v. The corresponding eigenvector (column of $\mathbf{C}$) gives the direction of the strain ϵ_3. Strain values greater than 0 indicate a tension whereas a value of 0 indicates a stable element.

3.2 Application to the Experimental Data

In Fig. 4, the s_3 strains (Eq. 23) are visualized for the six different load steps (cross sections of the voxel data blended with a cross section of the color-coded tetrahedrons). The evolution of cracks is visible. The corresponding stress-displacement curve is shown in the work of (Lorenzoni et al., 2020).
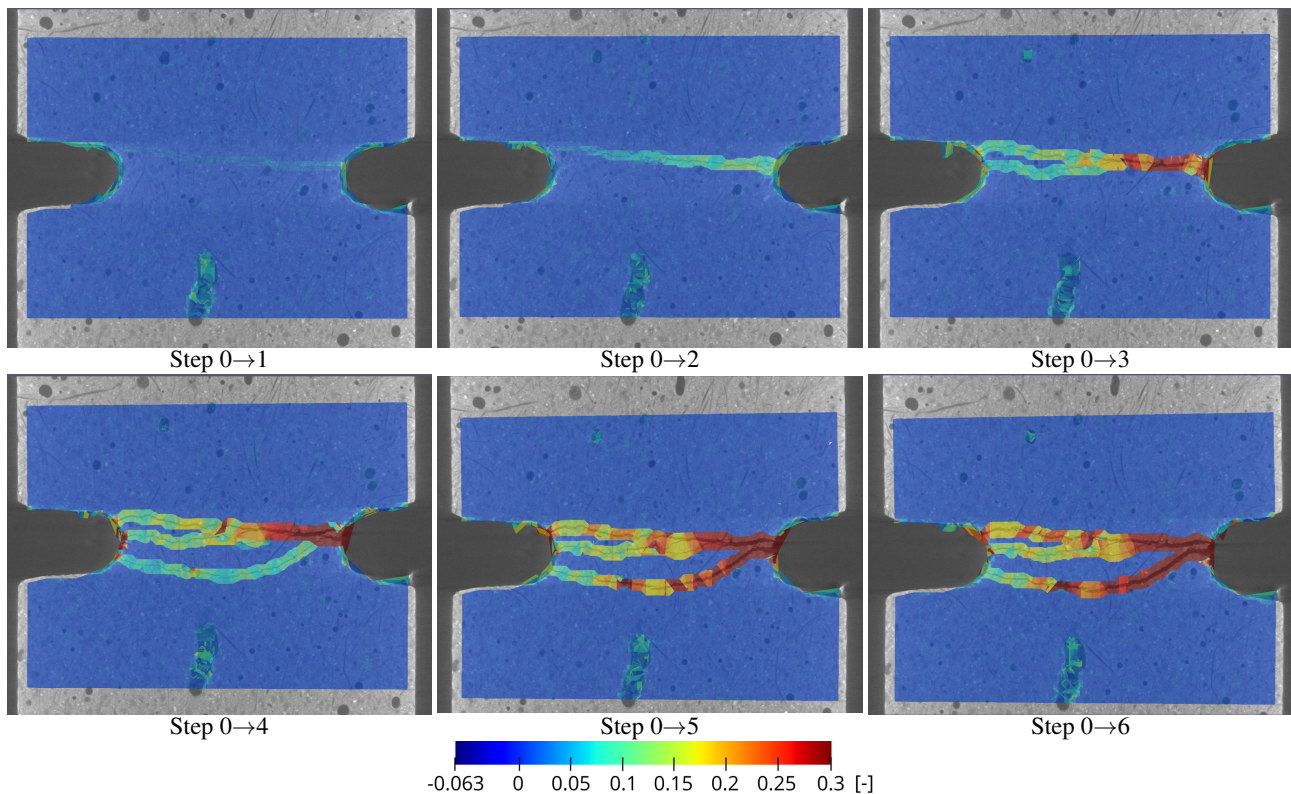
Figure 4. Slices of the voxel data blended with the cross-section of the s_3-color-coded tetrahedrons.

Especially, the visualization of step 5 shows some fluctuation in the strain values at the lower crack due to varying sizes of the tetrahedrons. It is a consequence of some missing matching results for points with matching cuboids crossed by the crack where LSM fails. In the lower center, some artefacts in the strain map are visible due to some matching errors at the air hole.

4. CONCLUSION

The paper presents the algorithm and application of 3D least squares matching to crack detection in multi-temporal micro-tomography voxel data sets. The affine parameters in the model allow to regard rotations and scaling between states. Changes in illumination are considered by radiometric parameters. Displacement vector fields are computed with standard deviations of the translation parameters of less than 0.02 vx. Strain values are calculated from the displacements to show deformed areas and to detect cracks.

Future work could concentrate on the determination of the accuracy of the 3D least squares matching.

ACKNOWLEDGEMENTS

REFERENCES

Ackermann, F., 1984. Digital Image Correlation: Performance and Potential Application in Photogrammetry. *The Photogrammetric Record*, 11(64), 429–439.

Altenbach, H., 2018. *Kontinuumsmechanik*. 4 edn, Springer Vieweg.

Barazzetti, L., Scaioni, M., 2010. Development and Implementation of Image-based Algorithms for Measurement of Deformations in Material Testing. *Sensors*, 10, 7469–7495.

Barnea, D. I., Silverman, H. F., 1972. A Class of Algorithms for Fast Digital Image Registration. *IEEE Transactions on Computers*, C-21(2), 179-186.

Bay, B. K., Smith, T. S., Fyhrie, D. P., Saad, M., 1999. Digital volume correlation: Three-dimensional strain mapping using X-ray tomography. *Experimental Mechanics*, 39, 217–226.

Becker, E., Bürger, W., 1975. *Kontinuumsmechanik*. 20, 1 edn, Vieweg+Teubner Verlag.

Grün, A., 1985. Adaptive least squares correlation: a powerful image matching technique. *South African Journal of Photogrammetry, Remote Sensing and Cartography*, 14(3), 175–187.

Hampel, U., Maas, H.-G., 2003. Application of digital photogrammetry for measuring deformation and cracks during load tests in civil engineering material testing. *Proceedings of Optical 3-D Measurement Techniques VI*, 2, A. Grün, 80–88.

Hampel, U., Maas, H.-G., 2009. Cascaded image analysis for dynamic crack detection in material testing. *ISPRS Journal of Photogrammetry and Remote Sensing*, 64(4), 345–350.

Koschitzki, R., Schacht, G., Schneider, D., Marx, S., Maas, H.-G., 2011. Integration of photogrammetry and acoustic emission analysis for assessing concrete structures during loading tests. *Proceedings of SPIE Optical Metrology*, 8085, International Society for Optics and Photonics.

Liebold, F., Heravi, A. A., Mosig, O., Curbach, M., Mechtcherine, V., Maas, H.-G., 2020a. Crack Propagation Velocity Determination by High-speed Camera Image Sequence Processing. *Materials*, 13(19).

Liebold, F., Maas, H.-G., 2016. Advanced spatio-temporal filtering techniques for photogrammetric image sequence analysis in civil engineering material testing. *ISPRS Journal of Photogrammetry and Remote Sensing*, 111, 13–21.

Liebold, F., Maas, H.-G., 2018. Sub-pixel accuracy crack width determination on concrete beams in load tests by triangle mesh geometry analysis. *ISPRS Annals of Photogrammetry, Remote Sensing and Spatial Information Sciences*, IV-2, 193–200.

Liebold, F., Maas, H.-G., 2020. Strategy for Crack Width Measurement of Multiple Crack Patterns in Civil Engineering Material Testing using a Monocular Image Sequence Analysis. *PFG – Journal of Photogrammetry, Remote Sensing and Geoinformation Science*, 88(3), 219–238.

Liebold, F., Maas, H.-G., Deutsch, J., 2020b. Photogrammetric determination of 3D crack opening vectors from 3D displacement fields. *ISPRS Journal of Photogrammetry and Remote Sensing*, 164, 1 - 10.

Liebold, F., Maas, H.-G., Heravi, A. A., 2019. Crack Width Measurement for Non-planar Surfaces by Triangle Mesh Analysis in Civil Engineering Material Testing. *International Archives of Photogrammetry, Remote Sensing and Spatial Information Sciences*, XLII-2/W18, 107–113.

Lorenzoni, R., Curosu, I., Léonard, F., Paciornik, S., Mechtcherine, V., Silva, F. A., Bruno, G., 2020. Combined mechanical and 3D-microstructural analysis of strain-hardening cement-based composites (SHCC) by in-situ X-ray microtomography. *Cement and Concrete Research*, 136, 106139.

Lucas, B. D., Kanade, T., 1981. An iterative image registration technique with an application to stereo vision. *Proceedings of the 7th International Joint Conference on Artificial Intelligence*, 2, 675–679.

Maas, H.-G., Hampel, U., 2006. Photogrammetric Techniques in Civil Engineering Material Testing and Structure Monitoring. *Photogrammetric Engineering and Remote Sensing*, 72(1), 39–45.

Maas, H.-G., Stefanidis, A., Grün, A., 1994. From pixels to voxels: tracking volume elements in sequences of 3D digital images. *International Archives of Photogrammetry, Remote Sensing and Spatial Information Sciences*, XXX-3/2, 539–546.

Ogden, R., 1997. *Non-linear Elastic Deformations*. 2 edn, Dover Publications.

Sutton, M. A., Orteu, J. J., Schreier, H., 2009. *Image Correlation for Shape, Motion and Deformation Measurements : Basic Concepts, Theory and Applications*. 1 edn, Springer.